

Improved Global Estimates of Terrestrial Evapotranspiration Using the MODIS and VIIRS Sensors

K. ARTHUR ENDSLEY^a, MAOSHENG ZHAO,^{b,c} JOHN S. KIMBALL,^a TYLER ALBRETHSEN,^a
AND SADASHIVA DEVADIGA^c

^a *Numerical Terradynamic Simulation Group, University of Montana, Missoula, Montana*

^b *Science Systems and Applications, Lanham, Maryland*

^c *Terrestrial Information Systems Laboratory, NASA Goddard Space Flight Center, Greenbelt, Maryland*

(Manuscript received 30 October 2024, in final form 28 January 2025, accepted 21 March 2025)

ABSTRACT: Terrestrial evapotranspiration (ET), as the link between water, energy, and carbon cycles, is key to understanding climate impacts on freshwater availability, agricultural yields, and forest mortality. Earth-observing sensors, such as the Moderate Resolution Imaging Spectroradiometer (MODIS) carried by NASA's Earth Observing System (EOS), are well suited to the study of ET at regional to global scales. As the era of EOS comes to a close, we present a comprehensive calibration and validation of the latest MODIS MOD16 ET product as well as new ET estimates based on data from the Visible Infrared Imaging Radiometer Suite (VIIRS) sensor, which is very similar to MODIS and is carried by the *Suomi NPP* and *NOAA-20* satellites, to continue the now 25-yr record of ET estimates from MOD16. Substantial updates and improvements to MOD16 are reported for the first time in over a decade of widespread use. Ground data sources including tower latent heat fluxes and plant traits are used in a Bayesian model-data fusion to constrain MODIS- and VIIRS-based ET estimates. Independent validation against sapflow and tower data shows that the resulting products have lower absolute bias and higher accuracy than the current MOD16 Collection 6.1 product. While MOD16 underestimates cropland ET, an intercomparison with the OpenET suite of models indicates that the improved MOD16 has the lowest error, lowest absolute bias, and highest model efficiency at noncropland sites. In combination with MODIS primary productivity estimates, these updates to MOD16 ensure the continuity of multidecadal ET and water-use efficiency estimates through 2030 or later.

KEYWORDS: Evapotranspiration; Hydrologic cycle; Hydrologic models; Ecological models; Remote sensing; Atmosphere-land interaction

1. Introduction

Major interest in terrestrial evapotranspiration (ET, the sum of evaporated surface water and water vapor transpired by plants) has been motivated, in part, by its magnitude: After precipitation, ET is the second largest flux in the water cycle over land, returning almost two-thirds of terrestrial precipitation to the atmosphere (Oki and Kanae 2006; Trenberth et al. 2007) by consuming the majority of available solar energy at the surface (Wild et al. 2013), thereby linking the global water and energy cycles. As ongoing climate warming increases the amount of water the atmosphere can hold (Huntington 2006), the horizontal transfer of water vapor and concomitant changes in aridity are uncertain (Greve et al. 2014; Miralles et al. 2014; Huang et al. 2016) despite the significant consequences for freshwater availability to terrestrial ecosystems and human communities. But ET is also of interest because it links the water cycle to the global carbon cycle (Zhang et al. 2015; Yang et al. 2023). The loss of water (through plant stomata) necessary for carbon gain fundamentally links ET (as transpiration) and vegetation carbon uptake. Changes in the efficiency of water-

for-carbon [water-use efficiency (WUE)] may ultimately determine changes in woody plant mortality, agricultural yields, and, again, changes in water supplies (Xu et al. 2019; McDowell et al. 2022).

ET is driven by Earth's surface energy balance and mediated by the state of the near-surface atmosphere, the wetness of surface soils, and the extent and type of surface vegetation. As such, it is a quantity that is well-suited for study by Earth-observing satellites, including NASA's Earth Observing System's (EOS) (Justice et al. 2002) *Terra* and *Aqua* satellites, which have carried the Moderate Resolution Imaging Spectroradiometer (MODIS) sensor for over two decades. MODIS data on surface albedo, leaf area index (LAI), and vegetation cover have enabled global, annual estimates of ET or potential ET and weekly estimates of latent heat flux from the MODIS MOD16 product (Mu et al. 2007, 2011) for nearly 25 years. MOD16 ET has been used to define planetary boundaries (Newbold et al. 2016), to quantify global water availability (Zhang et al. 2023; Bhattarai et al. 2023), to study the climate resilience of world ecosystems (Seddon et al. 2016), and to analyze the contribution of forests and vegetation change to the planet's surface energy balance (Li et al. 2015; Duveiller et al. 2018). The product's low latency, moderate resolution (500 m), and global extent have enabled its frequent inclusion in global meta-analyses and ensemble modeling (e.g., Liang et al. 2021; Yang et al. 2023).

Although it has been operational and seen widespread use for almost two decades, MOD16's last major improvement (Mu et al. 2011) used a limited network of just 46 eddy covariance (EC) towers to constrain the model's predictions. In that

Supplemental information related to this paper is available at the Journals Online website: <https://doi.org/10.1175/JHM-D-24-0145.s1>.

Corresponding author: Maosheng Zhao, maosheng.zhao@nasa.gov

DOI: 10.1175/JHM-D-24-0145.1

© 2025 American Meteorological Society. This published article is licensed under the terms of the default AMS reuse license. For information regarding reuse of this content and general copyright information, consult the AMS Copyright Policy (www.ametsoc.org/PUBSReuseLicenses).

TABLE 1. Commonly used abbreviations in this paper, followed by the abbreviations used for PFTs.

Abbreviation	Description
EC	Eddy covariance, referring to EC towers that measure latent heat flux
C61	MODIS Collection 6.1, the most recent version of MODIS data products
C61-UG	MODIS MOD16 Collection 6.1 User Guide
fPAR	Fraction of PAR absorbed by the canopy, i.e., fraction of the ground that is covered by canopy
GEOS	Goddard Earth Observing System, the land surface model providing surface meteorology data to MOD16
GEOS-IT	GEOS for Instrument Teams, a specific product of the GEOS land surface model
GLEAM	Global Land Evaporation Amsterdam Model (Miralles et al. 2025)
GPP	Gross primary productivity, the total carbon uptake of an ecosystem
λE	Latent heat flux, the product of the latent heat of vaporization λ and the mass flux of water E
KGE	Kling–Gupta efficiency
LAI	Leaf area index, the amount of leaf area per unit ground area as seen from above
MCD12Q1	MODIS-based land-cover product, an input to MOD16 and VNP16
MCMC	Markov chain Monte Carlo
MODIS	Moderate Resolution Imaging Spectroradiometer
MOD15A2H	The MODIS fPAR and LAI data product, an input to MOD16
MOD16	Satellite-based ET data product, originally using MODIS data only
MOD16A3HGF	The year-end, gap-filled annual ET product from MODIS MOD16
MCD43A3	The MODIS-based surface albedo product, an input to MOD16
PAR	Photosynthetically active radiation
PM	Penman–Monteith, a methodology for computing ET
PFT	Plant functional type
RMSE	Root-mean-square error
<i>SNPP</i>	<i>Suomi National Polar-Orbiting Partnership</i> , a satellite carrying the VIIRS sensor
SVP	Saturated vapor pressure, the vapor pressure when the air is saturated with water
TRY	The global TRY database of plant traits (Kattge et al. 2020)
T/ET	The transpiration T fraction of total ET
E_{canopy}/ET	The canopy evaporation fraction of total ET
E_{soil}/ET	The soil evaporation fraction of total ET
VIIRS	Visible Infrared Imaging Radiometer Suite
VNP15A2H	The VIIRS fPAR and LAI data product, an input to VNP16
VNP16	Satellite-based ET data product using VIIRS data from the <i>SNPP</i> satellite
VNP43MA3	The VIIRS-based surface albedo product, an input to VNP16
VPD	Vapor pressure deficit, a measure of the dryness of the air
WUE	Water-use efficiency (the GPP:ET ratio)
ENF	Evergreen needleleaf forest
EBF	Evergreen broadleaf forest
DNF	Deciduous needleleaf forest
DBF	Deciduous broadleaf forest
MF	Mixed forest
CSH	Closed shrubland
OSH	Open shrubland
WSV	Woody savanna
SAV	Savanna
GRS	Grassland
CRO	Cropland

time, the MODIS data archive has grown, as have global databases of EC tower fluxes ([Poyatos et al. 2021](#)) and other ground-based measurements (e.g., [Kattge et al. 2020](#)). The most recent version, MOD16 Collection 6.1 (C61), was calibrated using MODIS Collection 5 data, which are now obsolete. The MOD16 algorithm has also changed; this paper is the first published description of the current, operational algorithm since [Mu et al. \(2011\)](#). And now, the longevity of MOD16's multidecadal ET and latent heat flux data is imperiled by the end of the *Terra* and *Aqua* satellite missions. Data from the Visible Infrared Imaging Radiometer Suite (VIIRS) sensor aboard the *Suomi National Polar-Orbiting Partnership* (*SNPP*) and *NOAA-20* satellites are being used to ensure the

continuity of MODIS products ([Endsley et al. 2023](#); [Román et al. 2024](#)) and may enable MOD16 ET estimates to reach a 30-yr record, or longer. Here, we describe the updated MOD16 algorithm (Table 1 serves as a guide to abbreviations) as well as a comprehensive calibration and validation (Cal–Val) of MOD16 and the development of a new VIIRS VNP16 ET product.

2. Data and methods

Despite the long history and widespread application of MOD16, but perhaps because of its complexity, previous descriptions of the model suffer from inaccuracies or obsolescence.

TABLE 2. MOD16 model parameters, in a common notation used in this paper, based on the original table in Endsley (2024).

Parameter	Description
$T_{\min, \text{close}}$	Temperature at which stomata are almost completely closed ($^{\circ}\text{C}$)
$T_{\min, \text{open}}$	Temperature at which stomata are almost fully opened ($^{\circ}\text{C}$)
$\text{VPD}_{\text{close}}$	VPD at which stomata are almost completely closed (Pa)
VPD_{open}	VPD at which stomata are almost completely opened (Pa)
g_{SH}	Leaf conductance to sensible heat per unit LAI ($\text{m s}^{-1} \text{LAI}^{-1}$)
g_{wv}	Leaf cond. to evaporated water per unit LAI ($\text{m s}^{-1} \text{LAI}^{-1}$)
$g_{\text{cuticular}}$	Leaf cuticular conductance (m s^{-1})
C_L	Mean potential stomatal conductance per unit leaf area (m s^{-1})
$r_{\text{BL}, \text{min}}$	Minimum atmospheric boundary layer resistance (s m^{-1})
$r_{\text{BL}, \text{max}}$	Maximum atmospheric boundary layer resistance (s m^{-1})
B	Soil moisture constraint on potential soil evaporation

Consequently, previous descriptions are inconsistent with the operational product originally developed by Mu et al. (2007, 2011). A complete, up-to-date model description is available in the software documentation of the open-source Python implementation (Endsley 2024). Here, we correct and update previous model descriptions using the MOD16 C61 User Guide (Running et al. 2021) (hereafter, “C61-UG”) as a starting point. The C61-UG does provide an accurate, flowchart representation of the MOD16 algorithm (C61-UG, Fig. 2). For consistency and clarity, Table 2 delineates the parameters of the model. The new VIIRS VNP16 product uses the same MOD16 algorithm and parameters, but it is driven by canopy and surface albedo observations from VIIRS instead of MODIS.

a. The MOD16 algorithm

The purpose of MOD16 is the estimation of ET or, equivalently, of latent heat λE flux from the terrestrial surface to the atmosphere. The λE flux is just one of the components of the surface energy balance, along with sensible heat H , ground heat flux G , the change in heat storage ΔS , and their total, which is the net radiation intercepted by Earth’s surface R ,

$$R = H + \lambda E + G + \Delta S. \tag{1}$$

Here, λE is the amount of heat that has been used to vaporize (or evaporate) water. MOD16 uses the Penman–Monteith (PM) approach to modeling evaporation (Cleugh et al. 2007; Mu et al. 2007), which is based on two key ideas (Monteith 1965). First, the conservation of energy is used to determine how much (solar and thermal) energy is available to vaporize water. Second, the saturation vapor pressure (SVP) of the air is used to determine when to stop vaporizing water, i.e., when the air is saturated. These ideas were further developed into

calculations for the effective resistances to water vapor transport: the surface (or canopy) resistance, which describes the (inverse rate of) diffusion of water from the source (e.g., pure soil water or a turgid leaf mesophyll) to the evaporative front; and the aerodynamic resistance, which is chiefly the (inverse rate of) diffusion of water vapor into the free air (van de Griend and Owe 1994).

MOD16 simplified the calculation of surface resistance by using remotely sensed observations of the vegetation canopy (Cleugh et al. 2007), which ultimately enabled partitioning of the λE flux further into evaporation from bare soil surfaces and the evaporation and transpiration from wet canopy (Mu et al. 2007; K. Zhang et al. 2016). In the original MOD16 algorithm (Mu et al. 2007), the vegetation canopy observations [LAI and the fraction of photosynthetically active radiation (fPAR)] were derived from the MODIS sensor aboard the Terra and Aqua satellites. Because of the presence of clouds, daily MODIS data at 1-km resolution (later, at 500-m resolution) were composited into 8-day maximum-value composites (Myneni et al. 2002); hence, MOD16 ET estimates were also provided as an average over 8-day periods. The other MODIS input to MOD16 is the surface albedo, which is based on 16-day composites at 500-m resolution (Schaaf et al. 2018).

Fundamentally, the model estimates the 8-day λE flux as the sum of bare soil evaporation, evaporation from wet canopy, and transpiration (Mu et al. 2011). MOD16 is calibrated against the daily average λE flux measured at EC towers. While this flux cannot be partitioned into transpiration or soil or canopy evaporation, the total of these constituent daytime and nighttime fluxes estimated by MOD16 are compared to tower observations during calibration.

Calculating each component of ET (soil evaporation, canopy evaporation, and transpiration) begins with partitioning the net energy at Earth’s surface A [Eq. (3)], and, in all versions of MOD16, the net radiation at the canopy A_{canopy} or soil A_{soil} drives the rate of λE flux from vegetation or soil, respectively. This partitioning is determined by canopy fPAR and, in the case of A_{soil} , by G . Then, each component of ET is calculated based on an elaboration of the PM equation (Monteith 1965):

$$\lambda E = \frac{sA + \rho C_p (e_{\text{sat}} - e)(r_A)^{-1}}{s + \gamma [1 + r_s (r_A)^{-1}]}, \tag{2}$$

where $e_{\text{sat}} - e$ is the vapor pressure deficit (VPD) or difference between saturated e_{sat} and actual e vapor pressure; s is the slope of the e_{sat} curve; ρC_p , the product of air density ρ and air’s specific heat capacity C_p , is the heat storage capacity of the air; γ is the psychrometric constant, relating e to temperature; and r_A and r_s are the aerodynamic and surface resistances to latent heat flux, respectively (Endsley 2024). Each component of λE is computed based on Eq. (2), and each is proportional to $(sA + 1)/(s + 1)$, exchanging radiation and resistance terms depending on the component. The calculation of transpiration exchanges A for A_{canopy} , computes r_A differently, and includes canopy resistance [Eq. (5)]. The calculation of (potential) soil evaporation exchanges A for A_{soil}

[Eq. (6)], and the resistance terms account for the resistance to water movement through the soil column and near-surface air [Eq. (7)]. The calculation of canopy evaporation exchanges A for A_{canopy} , and is described in full by Mu et al. (2011). A full description of the MOD16 algorithm is available in Endsley (2024).

Transpiration is also driven by the LAI, daily minimum temperature T_{min} , and VPD; the key quantity for estimating transpiration is the surface conductance, which is based on a potential stomatal conductance C_L that is reduced under limiting conditions (low T_{min} or high VPD) according to four parameters (see Table 2); these describe linear functions that convert T_{min} and VPD into scalars between zero (stomata completely closed and conductance fully limited) and one (stomata completely open). Cuticular conductance $g_{\text{cuticular}}$ is a minor contribution to transpiration. Evaporation from wet canopy is driven by VPD but also inhibited by the resistance to water vapor transport g_{wv} and the parallel resistances to radiative heat transfer and sensible heat transfer g_{SH} . Evaporation from bare soil is primarily a function of VPD and the combined surface and aerodynamic resistances. The combined resistance increases with increasing VPD (according to a linear ramp function bounded by $r_{\text{BL,min}}$ and $r_{\text{BL,max}}$) because it is assumed that the near-surface air is in equilibrium with the soil surface; hence, the drier the air, the drier the soil.

b. Differences between MODIS and VIIRS ET data products

As two different EOS satellites carry MODIS sensors, the MODIS-based MOD16 data products are produced using data from either *Terra* (products with names beginning “MOD16”) or *Aqua* (names beginning “MYD16”). The *Terra* satellite’s original orbit was designed such that it crossed the equator at the same mean local time (MLT), 1030 MLT; for *Aqua*, this was 1330 MLT, which accounts for the primary difference between *Terra* and *Aqua* data products. As *Terra* and *Aqua* have both exceeded their design life and their orbits are now drifting, the equatorial MLT is also changing (Román et al. 2024), which partly motivates the development of new MOD16-based estimates, using data from a different source.

With the launch of the VIIRS sensor aboard *SNPP* in 2012, new LAI and fPAR data became available with the same spatial and temporal resolutions as the corresponding MODIS data (Myneni and Knyazikhin 2018). The VIIRS sensor is very similar to MODIS, and while the spectral bands and their calibrations do differ, the LAI and fPAR data produced by MODIS and VIIRS are very consistent (Xu et al. 2018; Yan et al. 2021), with some caveats. First, the *SNPP* and *NOAA-20* satellites that carry VIIRS also have an equatorial MLT of 1330 MLT. In the humid tropics, solar insolation (driving ET) tends to produce more clouds as the day progresses, leading to cloudier conditions in the afternoon than in the morning. This results in lower-quality retrievals of vegetation canopy parameters such as fPAR and LAI (Xu et al. 2018), which would be filled with seasonal-average values (or, in the gap-filled product, with values from a nearby date) more often.

MODIS also has better performance at high LAI values (Yan et al. 2021).

Similarly, the detection of clouds and other low-quality conditions is hampered in the VIIRS products (Yan et al. 2021). These differences mean that VIIRS fPAR and LAI show greater deviations from MODIS over relatively dense tropical canopies like evergreen broadleaf forest (EBF). The 8-day compositing and the difference in the effective pixel size at the edges of an image (due to off-nadir viewing angles) are other sources of difference between MODIS and VIIRS fPAR and LAI retrievals (Yan et al. 2021) that likely effect all regions and biomes. The MODIS and VIIRS albedo products (MCD43A3 and VNP43M, respectively), on the other hand, show strong consistency (Liu et al. 2017) and, while the two specific albedo products used in MOD16 and VNP16 were not directly compared, both have effective spatial resolutions (i.e., at any view angle) of less than 1 km (Campagnolo et al. 2016).

For these reasons, and because long-term assessments of ET spanning both generations of sensors are certainly needed (Román et al. 2024), we assessed whether bias exists between MODIS MOD16 and VIIRS VNP16 ET estimates. To ensure the continuity of MOD16’s multidecadal record, we evaluated the suitability of VIIRS shortwave albedo (VNP43MA3; Schaaf et al. 2018) and VIIRS LAI and fPAR (VNP15A2H; Myneni and Knyazikhin 2018) for producing a new VIIRS ET product (VNP16) using the same MOD16 algorithm. Because MOD16 ET is a downstream product of the MODIS (or VIIRS) land product suite, integrating MODIS (or VIIRS) data with a physical model, it is less affected by the aforementioned differences between sensors. Therefore, we first evaluated the impact from using VIIRS data on modeled ET performance in the updated MOD16 model; i.e., with the same Biome Properties Lookup Table (BPLUT) as the recalibrated MOD16 but using VIIRS instead of MODIS data in the forward simulation.

c. Updates to MOD16 and the algorithm description

Since the publication of Mu et al. (2011), the operational MOD16 product has seen improvements made by NASA that have not been previously reported. First, the calculation of net radiation A is no longer based on surface emissivity [C61-UG, Eq. (7)] and is instead based on the sum of shortwave and longwave radiation:

$$A = (1 - \alpha)R_{\text{S}\downarrow} + R_{\text{L}}, \quad (3)$$

where $R_{\text{S}\downarrow}$ is the total downwelling, shortwave radiation ($\text{MJ m}^{-2} \text{day}^{-1}$); R_{L} is the net downward, longwave radiation ($\text{MJ m}^{-2} \text{day}^{-1}$); and α is the shortwave albedo under “black-sky” conditions. At night, $R_{\text{S}\downarrow}$ is assumed to be zero and so the net radiation is equal to R_{L} .

Air pressure (Pa) is still a (static) function depending only on elevation (Iribane and Godson 1981), as in the C61-UG but is simplified:

$$P_a = P_{\text{std}} \times (1 - \ell z T_{\text{std}}^{-1})^{5.256}, \quad (4)$$

where ℓ is the standard temperature lapse rate (0.0065 K m^{-1}), z is the elevation in meters, and P_{std} and T_{std} are the standard

pressure (101 325 Pa) and temperature (288.15 K) at sea level (Endsley 2024).

The calculation of canopy conductance to transpiration G_C (m s^{-1}) has also changed. It should now be calculated as a parallel conductance of leaf cuticular and stomatal components g_C and g_S , in series with leaf boundary layer conductance g_{BL} :

$$G_C = \frac{g_{BL}(g_S + g_C)}{g_{BL} + g_S + g_C} \quad \text{where} \quad g_{BL} = g_{sh}^l \times \text{LAI}(1 - F_{wet}), \quad (5)$$

where the LAI is the one-sided leaf area index, g_{sh}^l is the leaf conductance to sensible heat (per unit LAI), g_S is the stomatal conductance (m s^{-1}), g_C is the leaf cuticular conductance (m s^{-1}), and F_{wet} is the fraction of the surface that is inundated.

Previous model descriptions omitted details on the calculation of SVP, used in calculating humidity; SVP is calculated based on a form of the August–Roche–Magnus formula by Abbott and Tabony (1985) (cited by Alduchov and Eskridge 1996, their Table 1). The C61-UG also omits the details on the calculation of air density, which should be based on the

“simplified” formula from the National Institute of Standards and Technology (NIST, cited by National Physical Laboratory 2002).

There are also errors in previous publications that need to be addressed. In the MOD16 C61-UG, in calculating net radiation received by the soil A_{soil} [Eq. (8)], it is suggested that only net radiation is modulated by the bare soil area (represented as $1 - fPAR$, where $fPAR$ is the fraction of photosynthetically active radiation intercepted by the canopy). In fact, it is the difference between net radiation and the ground heat flux G that is modulated:

$$A_{soil} = (1 - fPAR) \times (A - G). \quad (6)$$

There is an error in both Mu et al. [2011, Eq. (26)] and in C61-UG [Eq. (19)] regarding the calculation of atmospheric boundary layer resistance, part of the soil evaporation calculation. This is a confusing part of the MOD16 algorithm because it intentionally combines aerodynamic and surface resistances into a bulk “boundary layer resistance” (s m^{-1}) and uses humidity as a proxy for the surface soil moisture content. That equation should be as follows:

$$r_{total} = r_{corr} \times \begin{cases} r_{BL,min} & \text{VPD} \leq \text{VPD}_{open} \\ r_{BL,max} - \frac{(r_{BL,max} - r_{BL,min})(\text{VPD}_{close} - \text{VPD})}{\text{VPD}_{close} - \text{VPD}_{open}} & \text{VPD}_{open} < \text{VPD} < \text{VPD}_{close} \\ r_{BL,max} & \text{VPD} \geq \text{VPD}_{open} \end{cases} \quad (7)$$

That is, boundary layer resistance r_{total} ought to be an increasing function of VPD, not a decreasing function, as implied in Mu et al. [2011, Eq. (26)]; other parameters are defined in Table 2. Previous publications (Mu et al. 2011, C61-UG) erroneously switched the terms $r_{BL,min}$ and $r_{BL,max}$.

These errors (in A_{soil} and r_{total}) are limited to previously published descriptions; they are not in the operational code and do not affect the performance of MOD16 C61 or any earlier product releases, but they may have affected other MOD16 implementations from the literature that are based on the C61-UG or Mu et al. (2011). These errors, changes to MOD16, or both might explain differences in the sensitivity and uncertainty analyses reported herein as compared to other recent studies (e.g., Zhang et al. 2019; Brust et al. 2021).

d. Model calibration procedure

Latent heat fluxes from 317 towers, worldwide, were compiled from the AmeriFlux and FLUXNET (Pastorello et al. 2020) collections (Table S13 in the online supplemental material). Half-hourly records of latent heat flux were aggregated to mean daily flux following the procedure described by Zhang et al. (2019). Specifically, the surface energy balance was calculated for each observation as the difference between net radiation and the sum of latent, sensible, and ground heat fluxes. Records where the imbalance was greater than $10 \text{ W m}^{-2} \text{ min}^{-1}$ were discarded. Records where any part of the energy budget (latent, sensible, or ground heat flux) was missing

were also discarded. Days with more than 6 h of missing data were not used; i.e., latent heat flux was aggregated, taking the mean, only for days with at least 36 half-hourly observations. In the fewer than 2% of cases where the mean daily heat flux was calculated to be negative, we assigned zero, as negative latent heat fluxes are generally associated with stable conditions under which EC measurements are less reliable (Paulus et al. 2024). An additional 34 towers, mostly in the United States, were removed from the calibration–validation (Cal–Val) dataset because of very high rates of missing or poor-quality data.

To compute predicted latent heat fluxes with MOD16 (to be compared to observed fluxes at towers), we compiled surface meteorological driver data from the NASA GMAO Goddard Earth Observing System (GEOS) for Instrument Teams (GEOS-IT), for each tower site. Air pressure in MOD16 is static for a given location and calculated based on elevation data from the 30-arc-s Shuttle Radar Topography Mission dataset (NASA-JPL 2013). While VPD, air temperature, air density, and relative humidity were calculated separately for daytime and nighttime, the minimum temperature is the daily minimum of hourly air temperature estimates. Canopy $fPAR$ and LAI were estimated at each tower site based on either the gap-filled MODIS MOD15A2H (Myneni et al. 2002) or VIIRS VNP15A2H product (Myneni and Knyazikhin 2018), where gap filling addresses missing data caused by unfavorable atmospheric conditions, such as cloud cover and aerosols

(Zhao et al. 2005). These 8-day estimates were sampled within a 3×3 pixel window (approximately 1.5-km footprint), centered on the tower, and then interpolated to daily time steps. Black-sky, shortwave albedo was estimated at each tower site based on either the MODIS MCD43A3 or VIIRS VNP43MA3 products (Schaaf and Wang 2021), using the same spatial sampling as for fPAR/LAI and the same interpolation to daily time steps.

Using these driver data and the tower latent heat fluxes, MOD16 was calibrated using Bayesian data fusion, where prior estimates of some MOD16 parameters (all except β and the T_{\min} and VPD parameters, see Table 2) were derived from multiple published sources, using maximum likelihood estimation (MLE) to fit lognormal distributions to the available data, given the right skew of conductance distributions. This approach to calibration is a commonly used alternative to numerical optimization (e.g., stochastic gradient descent) and is advantageous because it allows for disparate, prior data sources to be integrated and it provides a distribution of optimal parameter values, rather than a single point estimate. Model calibration was performed separately for each plant functional type (PFT, Table S1), based on the MODIS MCD12Q1 “type 2” land-cover classification (Friedl and Sulla-Menashe 2019; Sulla-Menashe et al. 2019). Details on the selection of priors for model-data fusion can be found in the supplemental material.

The model calibration was performed using Markov chain Monte Carlo (MCMC) with the Differential Evolution Metropolis sampler described by Ter Braak and Vrugt (2008), as implemented in the PyMC framework (Abril-Pla et al. 2023; Wiecki et al. 2024). A total of 20 000 samples were drawn from the posterior for each of three chains, based on a root-mean-square error (RMSE) pseudo-likelihood function, and chains were assessed in the manner described by Endsley (2024). We experimented with imposing an additional constraint on the objective function (RMSE), where an additional penalty was incurred if mean annual ET exceeded the mean annual precipitation (MAP) for a site, where MAP was determined by the IMERG-Final global precipitation product (NASA 2019). However, despite its theoretical value, this constraint did not improve postcalibration goodness-of-fit, so it was not used in producing the final results.

e. Model sensitivity analysis

The model sensitivity analysis performed followed closely the procedure of Endsley et al. (2023). The choice of bounds for parameters has a large effect on the results of this kind of sensitivity analysis. We chose physically meaningful bounds for each parameter based on the literature, similar to how prior distributions were defined (see the supplemental material). We also evaluated how changing some of the bounds affected the parameter sensitivity scores and found that it did not affect the ordering of parameters, by sensitivity score, within the top five parameters. In addition to a sensitivity analysis of the model parameters, we also evaluated the sensitivity of the model to the input drivers, using the same variance-based sensitivity framework, with the model parameters set to their average values across all PFTs.

f. Independent validation

For independent validation, some EC tower data were excluded from model calibration. We excluded between 9 and 40 site-years of data for each PFT, with the exception of closed shrubland (CSH), a PFT for which there were too few towers and, therefore, only 1 site-year could be spared. The structured random sample of site-years, within PFT classes, was based only on site-years where at least 97% of the year’s daily observations were valid. Initially, up to 25 site-years of data were excluded for each PFT, but additional towers within the contiguous United States (CONUS) were reserved to facilitate a better comparison with OpenET (see section 2g). Validation statistics were reported using only the excluded data and include RMSE, mean bias, Pearson correlation, and the Kling–Gupta efficiency (KGE; Gupta and Kling 2011). The KGE is a metric that balances the previous three statistics (RMSE, bias, and correlation) and is frequently used in hydrological studies because of the tendency for RMSE-based performance assessments to result in low variance of predictions; 1.0 is the highest (best) KGE score possible.

We also validated MOD16 and VNP16 estimates against sapflow measurements from the SAPFLUXNET database (Poyatos et al. 2021). Using the “sapfluxnet” package for R, we filtered out the sites that indicated some kind of management, drought or irrigation treatment, or CO₂ enrichment. Then, we computed 24-h daylight metrics using the provided aggregation function, computing the 50th percentile of daylight sapflow.

We then aggregated these individual-level sapflows, for each site, to a stand-level sap flux Q_{stand} following the procedure recommended by Poyatos et al. (2021):

$$Q_{\text{stand}} = A_{\text{stand}} \times \left(\sum_k f_k \frac{1}{N} \sum_{i \in k} \frac{Q_i}{A_i} \right), \quad (8)$$

where Q_i is the individual-level sapflow from the SAPFLUXNET database, aggregated to daily time steps; A_i and A_{stand} are the individual- and stand-level basal areas, respectively; N is the number of individuals of species k (K total species) that are found in that stand; and f_k is the proportion of the stand area represented by that species. Where f_k was missing from sites with only one species present, those records were assigned $f_k = 1.0$ (100%). After summing up sapflows for each time step at each site, records where the total summed area fraction (total f_k) was less than 0.95 (95%) were removed. We also filtered out sites with fewer than 30 time steps, to improve the quality of data for comparison. Because of the indirect relationship between sapflow and transpiration (Wullschleger et al. 2001), we decided to assess the relationship between daytime, stand-level sap fluxes Q_{stand} , and MOD16 daytime transpiration using only the Pearson correlation. When comparing to SAPFLUXNET sites, where we lacked GEOS-IT data, both MOD16 C61 and updated MOD16 ET estimates were generated using climate driver data from the publicly available Modern-Era Retrospective Analysis for Research and Applications, version 2 (MERRA-2; Gelaro et al. 2017), which has identical resolution and a similar climatology to GEOS-IT.

g. Global and regional comparisons

The partitioning of global and regional ET fluxes is critical for linking the carbon and water cycles. Partitioning is also a useful diagnostic for model performance because it can be constrained by observations (e.g., from isotope studies) and is widely reported in the prior literature. We calculated transpiration, soil evaporation, and canopy evaporation separately for each tower site in the Cal–Val dataset. These fluxes were then divided by their total within each PFT group. Global median values were calculated based on an area-weighted normalization, using each PFT's global land area proportion (Table S1) in the global MODIS MCD12Q1 type 2 map (Friedl and Sulla-Menashe 2019; Sulla-Menashe et al. 2019).

We also generated global maps of MOD16 and VNP16 ET at 5-km resolution using the updated algorithm and calibrated BPLUTs from this study (see section 2a) to verify model performance and consistency in representing global ET trends. The lower resolution (5 km) is necessitated by computational constraints and the long period of study. The resulting model trends were evaluated against other ET records obtained from the NASA MOD16 operational baseline (C61), gap-filled MOD16A3HGF product, and the Global Land Evaporation Amsterdam Model, version 4.1a (GLEAM v4.1a; Miralles et al. 2025), global, gridded product. Theil–Sen robust trends were used when calculating trends in annual ET over time. To highlight the strengths of MOD16 and its synergy with other MODIS products, we also computed ecosystem WUE as the ratio of MOD17 gross primary productivity (GPP) to updated MOD16 ET, where GPP is based on the global 5-km simulations in Endsley et al. (2023). WUE trends were assessed over the CONUS as a regional case study, evaluating cross-product consistency and potential synergy in clarifying dynamic trends in terrestrial water and carbon fluxes, and their linkages.

h. Comparisons with other models

Model-to-model comparisons are also useful for benchmarking model performance. OpenET is a model intercomparison project that runs an ensemble of ET models using field-scale data within the CONUS (Melton et al. 2022). The models include ALEXI/DisALEXI (Anderson et al. 2007, 2018), eeMETRIC (Kilic et al. 2021), geeSEBAL (Laipelt et al. 2021), PT-JPL (Fisher et al. 2008), SIMS (Melton et al. 2012), and SSEBop (Senay et al. 2023). We obtained monthly ET data for each OpenET model, and the ensemble mean where outliers were removed based on the mean absolute deviation (Volk et al. 2023a), covering the period 2001–20. The corresponding OpenET calibration and validation dataset (Volk et al. 2023b) contains EC tower fluxes for 71 sites in the CONUS that were not used in the MOD16 Cal–Val dataset. Of these 71 sites, only 61 have data from OpenET models due to the differences in coverage (Volk et al. 2024). For intercomparison with OpenET, daily MOD16 λE (W m^{-2}) estimates (from a 3×3 MODIS pixel footprint, approximately a 750 m radius centered on each tower location) were averaged over monthly time steps. OpenET and MOD16 were both

compared to the 61 independent tower records in terms of RMSE, correlation, bias, and KGE.

3. Results and discussion

Here, we describe the performance of the updated MODIS MOD16 (Collection 7) and the new VIIRS VNP16 (Collection 2) through independent validation and intercomparison with other datasets. This validation reflects improvements both to the model logic (see section 2c) and in the model parameters through calibration. As the operational MOD16 algorithm and its data products have been continuously updated by NASA, without peer-reviewed validation by its authors since the report of Mu et al. (2011), we cannot decompose the relative model improvement into its separate contributions from model logic and optimized parameters. However, we can report that the new air pressure calculation [Eq. (4)] produces values highly similar to those from our reanalysis data (not shown). The old calculation of net radiation [Mu et al. 2011, their Eq. (5)] produces R_L estimates that have lower variance than the R_L values from our reanalysis data [in Eq. (3)]; there is little consistency between the previously calculated values and the reanalysis values. And yet, the resulting ET estimates using either calculation of net radiation are very similar (root-mean-square deviation of 9.5 W m^{-2} , Pearson's $r = 0.986$).

a. Validation against tower latent heat fluxes

Validation against reserved, daily tower ET observations (i.e., data that were not used to calibrate C61 nor the updated MOD16) indicates that both the updated MODIS MOD16 and new VIIRS VNP16 improve upon the original MOD16 C61 (Table 3). RMSE and bias are both reduced, while spatiotemporal correlations and the model efficiency are both increased. RMSE in C61 is approximately $1.3 \text{ mm H}_2\text{O}$ per day, while in the updated MOD16, it is $1.1 \text{ mm H}_2\text{O}$ per day. The average bias in C61 amounts to $77 \text{ mm H}_2\text{O}$ per year in C61 but is reduced to $41 \text{ mm H}_2\text{O}$ per year in the updated MOD16. The overall bias reported masks significant variability in model bias among towers, ranging from -3.8×10^{-5} to $2.5 \times 10^{-5} \text{ mm H}_2\text{O s}^{-1}$ (2nd and 98th percentiles) in C61 and -3.1×10^{-5} to $2.7 \times 10^{-5} \text{ mm H}_2\text{O s}^{-1}$ in the updated MOD16. However, there is no trend in the bias with daytime VPD (Fig. S4); bias is generally lower in absolute magnitude at higher VPD.

When the performance of MOD16 is evaluated for specific PFTs (Table S2), we find that the updated MODIS MOD16 and new VIIRS VNP16 perform better than C61 for all PFTs except EBF, where performance is comparable to the older product (RMSE of 40.4 W m^{-2} in C61 compared to 41.2 for the updated MOD16). Similarly, while the newer products generally reduce the bias, for many PFTs, the bias is quite similar to C61 (Table S3). Notably, bias in EBF was substantially reduced but still remains relatively high.

b. Validation against sapflow data

The overall Pearson's correlation (pooling all sites together) between MOD16 daytime ET and SAPFLUXNET

TABLE 3. The RMSE, median bias, Pearson's correlation, and KGE for each MOD16 variant. Higher KGE scores are better, and the highest possible score is 1.0. The RMSE and bias in hydrological units ($\text{mm H}_2\text{O s}^{-1}$) are estimated by dividing the RMSE and bias in radiation units (W m^{-2}) by the latent heat of vaporization, which is based on the average of daytime and nighttime temperatures from GEOS-IT. The bold text in each column identifies the best statistic.

	MODIS MOD16 C61	Updated MOD16	New VIIRS VNP16
RMSE (W m^{-2})	37.2	31.8	32.2
Bias (W m^{-2})	6.0	3.3	3.0
RMSE ($\text{mm H}_2\text{O day}^{-1}$)	1.30	1.11	1.13
Bias ($\text{mm H}_2\text{O day}^{-1}$)	0.212	0.113	0.103
Correlation	0.557	0.717	0.709
KGE	0.450	0.696	0.685

median daytime sapflows ranges from 0.27 to 0.29, the latter achieved by removing 40 SAPFLUXNET sites with short records (less than 1 year). However, the overall correlation improves to 0.34 when comparing sapflows to MOD16 daytime transpiration, regardless of whether low-quality SAPFLUXNET sites are included. These low correlations elide significant variability among PFTs. Indeed, when PFTs are evaluated separately, correlations with daytime transpiration range from 0.28 (for EBF) to 0.76 [for mixed forest (MF), Table S4].

Acknowledging the significant variability in site characteristics, we further normalized the sapflows and transpiration fluxes by their respective, site-level, long-term mean and standard deviation, resulting in PFT-specific correlations ranging between 0.50 [for deciduous needleleaf forest (DNF)] and 0.77 (for MF, Fig. 1 and Table S5), excluding woody savanna (WSV), where the correlation is unexpectedly low ($r = 0.26$). These correlations are similar for C61, except in the case of DNF, where C61 performs best, and in savanna (SAV), where the updated BPLUT performs best (Table S5). The poor performance in WSV can be attributed to MOD16 consistently underestimating sapflows in winter and a general phase offset between MOD16 daytime transpiration and sapflow (Fig. S5). However, it should be noted that only three of the seven WSV sites from SAPFLUXNET provided data for at least one entire year; and those three sites are in close proximity to one another.

c. Intercomparison with OpenET

When compared at reserved EC tower sites within the CONUS, in non-cropland sites, the updated MOD16 displays lower RMSE, lower bias, and higher model efficiency (KGE) than any of the models in the OpenET ensemble (Table 4). MOD16 bias in non-cropland sites is significantly lower than the other models. MOD16 correlation with non-cropland latent heat fluxes is lower than some models, likely because MOD16 underestimates the largest observed fluxes. When performance is examined separately for each PFT (Table S6), we find that while MOD16 underperforms in croplands (CRO), MOD16 outperforms the other models in predicting latent heat fluxes for deciduous broadleaf forests (DBFs) and SAV, and is among the best models for grasslands (GRS) and shrublands. These differences are largely expected, as MOD16's relatively coarse spatial resolution and

lack of a water-supply constraint put it at a disadvantage in predicting croplands ET (He et al. 2019; Brust et al. 2021).

d. Sensitivity to model parameters and drivers

Sensitivity analysis reveals that the updated MOD16 ET estimates are mainly influenced by a few key model parameters (Fig. 2a). The leaf conductance to sensible heat g_{SH} accounts for over 70% of the variation in model ET estimates, likely because it is used in calculating both canopy evaporation and transpiration. In calculating transpiration, g_{SH} modulates the response of leaf boundary layer conductance to the LAI, an important driver of ET. The next most-important parameter is the mean potential stomatal conductance C_L , followed by the leaf conductance to water vapor g_{WV} and the minimum boundary layer resistance $r_{\text{BL,min}}$, although these last two parameters each explain less than 10% of the variation. The term g_{WV} is similar in magnitude (both in nature and in MOD16) to g_{SH} , but g_{WV} is used only to calculate the evaporation of canopy intercepted water. The term $r_{\text{BL,min}}$ is a somewhat sensitive parameter because it defines the lower bound of boundary layer resistance, which is experienced under low-to-moderate VPD. High VPD (>2500 Pa) is uncommon in our climate dataset, which means that the value of $r_{\text{BL,max}}$ rarely influences the output, hence the model's very low sensitivity to $r_{\text{BL,max}}$.

These results differ from the sensitivity analysis of Zhang et al. (2019), which found β , $r_{\text{BL,max}}$, and $r_{\text{BL,min}}$ to be highly sensitive parameters. This can partly be explained by the differences in the range of values allowed in the parameter sweep, and differences in the driver data used, and, otherwise, are likely a result of differences in model implementation (see section 2c). When model sensitivity is examined separately for each PFT (Fig. S3), we find that the effect of $\text{VPD}_{\text{close}}$, the VPD at which stomata are estimated to be almost completely closed, is significant for shrublands but has little impact on MOD16 estimates in other biomes. The term g_{WV} is a more sensitive parameter for EBFs and DBFs, respectively, implying a more significant role in the evaporation of intercepted water for those PFTs. Of course, PFTs experience different prevailing climate conditions, so the differences in $\text{VPD}_{\text{close}}$ and g_{WV} sensitivities might merely reflect differences in aridity (at tower sites). In terms of sensitivity to drivers, MOD16's estimates are dominated by daytime VPD, daytime air temperature, shortwave radiation, and daily minimum temperature

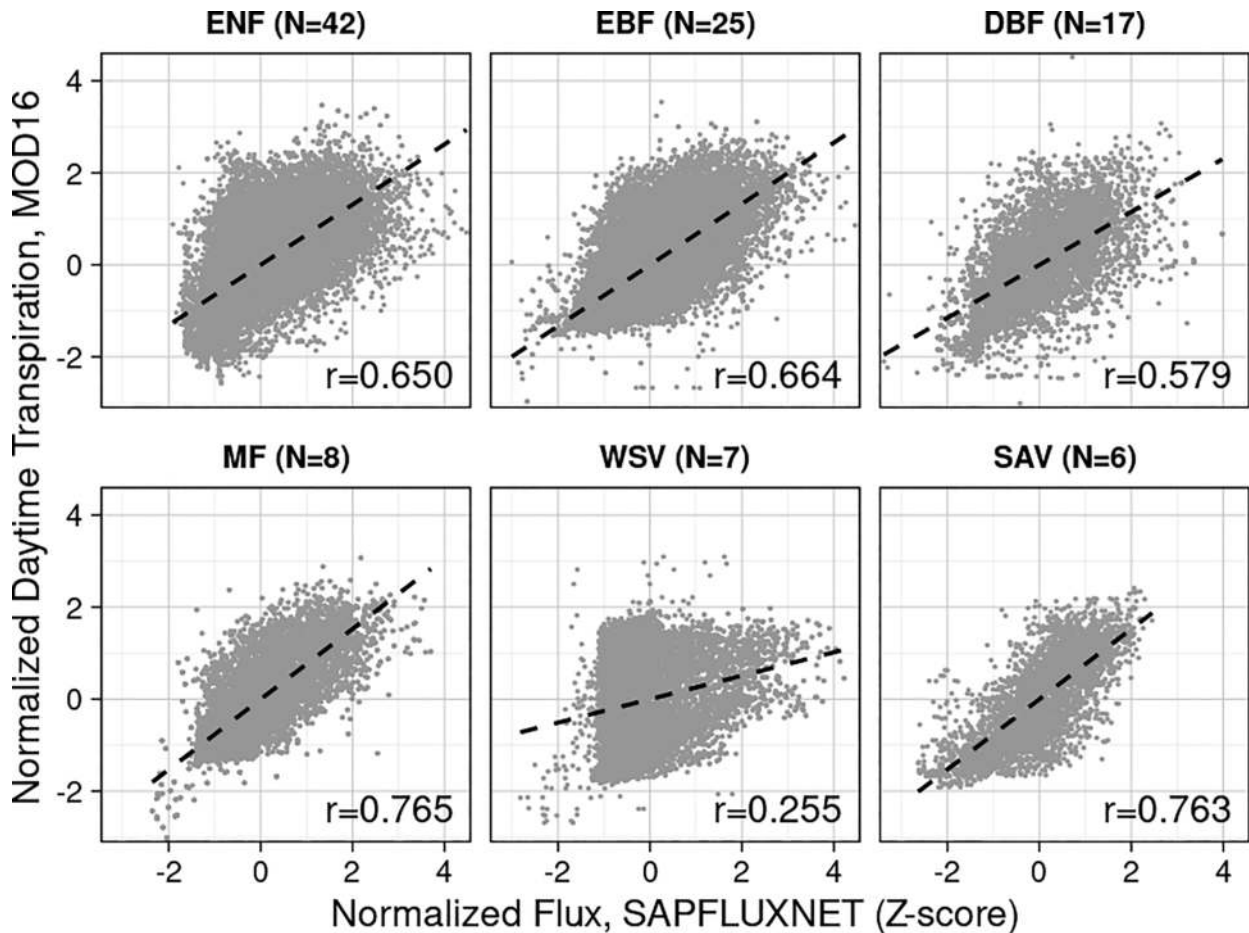


FIG. 1. Normalized daytime transpiration from MOD16 plotted against normalized sapflows from SAPFLUXNET, for each PFT, with Pearson’s correlation r and linear (dashed) trend line shown. The subplot label indicates the number of SAPFLUXNET sites N available for each PFT.

(Fig. 2b), consistent with our understanding of the primary drivers of ET.

e. Partitioning of ET

A major improvement to MOD16 is found in the partitioning of ET (Fig. 3). Previous work by Talsma et al. (2018) found that MOD16 and other ET models underestimate canopy transpiration and that MOD16, in particular, overestimates soil evaporation and significantly overestimates canopy interception. Consistent with the overall increase in transpiration-related parameters, the transpiration fraction of ET (T/ET) in the updated MOD16 is much higher than in C61 (Table S7). In the updated MOD16, the median T/ET across all towers in our Cal-Val dataset is 0.71, compared to 0.46 in MOD16 C61. The updated T/ET fractions are more realistic, compared with isotope-based partitioning, which points to a global average T/ET of 0.64 ± 0.13 and median T/ET of 0.65 (Good et al. 2015).

Our updated values for individual PFTs (Table S7) are also consistent with a reported global, median T/ET of 0.59 (Schlesinger and Jasechko 2014; Yang et al. 2023); with Berkelhammer et al. (2016), who reported T/ET values for needleleaf

forests between 0.5 and 0.6; and with Wei et al. (2017), who reported a global T/ET fraction of 0.57 ± 0.7 . In agreement with Zhou et al. (2016), we also found that T/ET is relatively high in croplands (0.69 compared to their 0.62–0.69) and is lowest for broadleaf forests (0.47–0.58 compared to their 0.52–0.56). Although there can be significant intra-annual variation in T/ET (Smith et al. 2018; Scott et al. 2021), the updated fractions represent a more realistic contribution of transpiration to total ET.

Partitioning of ET into soil evaporation E_{soil} and canopy interception E_{canopy} components is less common in the literature. However, given the results of Talsma et al. (2018), we can report that the updated MOD16 provides more realistic soil evaporation magnitudes, based on the E_{soil}/ET fraction (Table S8). Soil evaporation, and consequently E_{soil}/ET , was significantly overestimated in MOD16 C61 for most PFTs, with a median E_{soil}/ET in the training dataset of 0.42. In the updated MOD16, the median E_{soil}/ET across PFTs is 0.16 (0.15 in VIIRS VNP16), which is low but closer to the range of 0.2–0.3 proposed by Yang et al. (2023). The updated E_{soil}/ET fractions also compare well with those of Rigden et al. (2018), who found that the total evaporation fraction (including E_{soil}/ET and

TABLE 4. Performance metrics for the updated MOD16 and the ET models used in OpenET, including the OpenET ensemble mean: RMSE ($\text{mm H}_2\text{O month}^{-1}$), bias ($\text{mm H}_2\text{O month}^{-1}$), Pearson's correlation, and KGE. Performance is summarized for croplands and all non-cropland types. Estimates from SIMS were not available for non-cropland sites. The bold text in each column identifies the best statistic.

Model	Group	RMSE	Bias	Correlation	KGE
MOD16	Non-cropland	23.9	+2.3	0.82	0.78
DisALEXI	Non-cropland	28.8	+10.6	0.85	0.61
eeMETRIC	Non-cropland	30.5	+8.0	0.83	0.60
geeSEBAL	Non-cropland	39.4	+18.1	0.77	0.39
PT-JPL	Non-cropland	29.6	+15.6	0.85	0.56
SSEBop	Non-cropland	27.0	+6.4	0.87	0.64
OpenET ensemble mean	Non-cropland	27.8	+10.9	0.86	0.62
MOD16	Cropland	38.4	-16.2	0.82	0.60
DisALEXI	Cropland	21.1	-2.4	0.95	0.89
eeMETRIC	Cropland	25.7	-2.7	0.92	0.88
geeSEBAL	Cropland	22.8	-4.8	0.93	0.91
PT-JPL	Cropland	19.6	-0.8	0.95	0.92
SIMS	Cropland	23.8	+8.5	0.93	0.87
SSEBop	Cropland	26.0	-3.8	0.94	0.80
OpenET ensemble mean	Cropland	18.0	-2.6	0.96	0.94

$E_{\text{canopy}}/\text{ET}$) was highest in evergreen needleleaf forest (ENF) (compared to second-highest, for $E_{\text{soil}}/\text{ET}$, among PFTs in our study).

The estimation of E_{canopy} , as a fraction of ET, is similar between C61 and the updated MOD16, with a global median $E_{\text{canopy}}/\text{ET}$ of 0.12 (0.11 in VIIRS VNP16), compared to 0.10

in MOD16 C61. Although $E_{\text{canopy}}/\text{ET}$ was previously thought to be high in MOD16 (Talsma et al. 2018), the updated values (Table S9) compare well with the range of 0.1–0.2 proposed by Yang et al. (2023). The E_{canopy} increased considerably for EBF and DNF, and might be too high for EBF, in particular, although high humidity and precipitation in EBF might justify

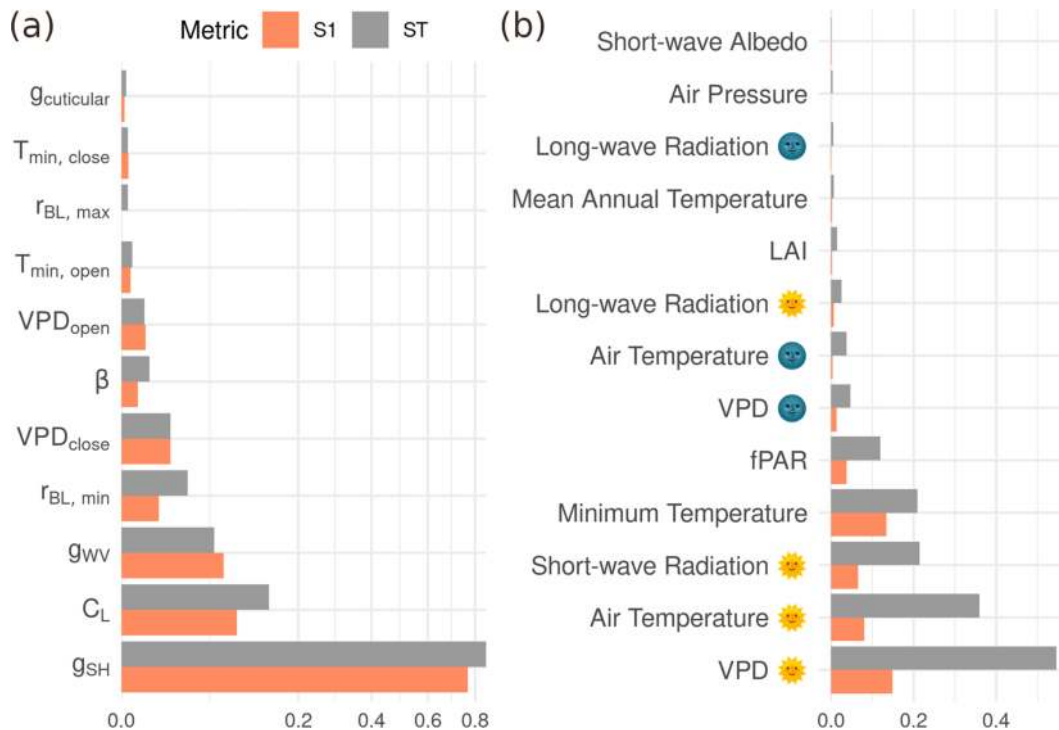


FIG. 2. Sensitivity analysis results for MOD16, showing model sensitivity (a) to internal parameters and (b) to input drivers. S1 refers to the direct effect of a parameter or driver on the modeled result, while ST refers to the effect after considering all interactions with other parameters or drivers. Sun and moon icons indicate the daytime and nighttime quantities, respectively.

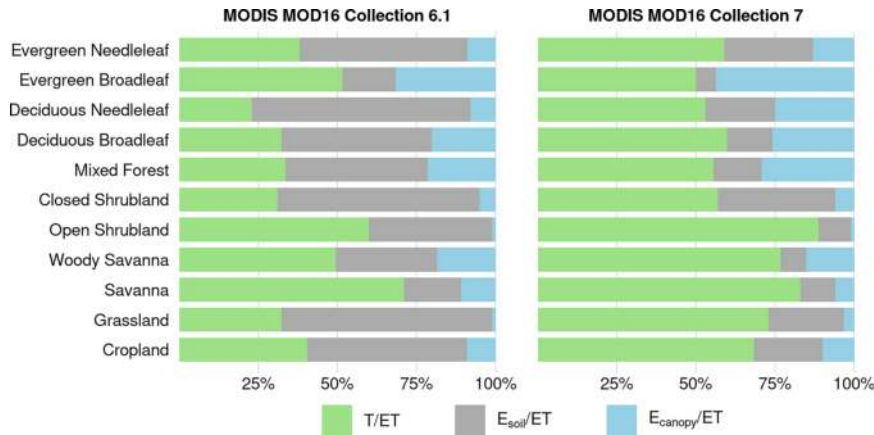


FIG. 3. The fractional components of ET in two versions of MODIS MOD16: the transpiration fraction of ET (T/ET), the soil evaporation fraction of ET (E_{soil}/ET), and the canopy evaporation fraction of ET (E_{canopy}/ET). Each fraction represents the median value across EC towers in the Cal–Val dataset.

a high rate of canopy interception and evaporation. Moreover, as pointed out by Yang et al. (2023), E_{canopy}/ET is expected to be higher in the tropical (generally EBF) and boreal (significant DBF and DNF) regions due to its relationship with LAI.

f. Continuity between MODIS and VIIRS

Based on the similar validation metrics between ET estimates produced using the same BPLUT but with VIIRS or MODIS input data (Table 3), and their highly similar partitioning of ET (Tables S7–S9), we conclude that there is almost no difference in ET performance between using MODIS or VIIRS input datasets. A particularly important question is whether there is a systematic difference, or bias, between MOD16 ET and VNP16 ET. We find that the overall bias is similar between MOD16 and VNP16 (Table 3) and, while PFT-specific analyses show some differences, the bias is of similar magnitude and in the same direction for each PFT (Table S3). Finally, we compared MOD16 and VNP16 time series ET data at select towers (not shown), for each PFT, and found no systematic differences. The forthcoming VNP16 product (expected in VIIRS Collection 2) is therefore expected to be comparable to the updated MOD16 product (expected in MODIS Collection 7).

g. Global patterns of ET

In the updated MOD16, mean annual ET for 2001–11 at the global scale is 521.0 mm yr^{-1} , which is very close to the value reported by Yang et al. (2023) of 520 ± 31 , compared to 568.8 in C61. Among different bioclimatic settings, the PFT with the highest mean annual ET (2001–11) in the updated MOD16 is EBF (1.12 m yr^{-1}), which compares well with the estimate of Yang et al. (2023) (1.23 m yr^{-1}) and is substantially reduced from C61 (1.40 m yr^{-1}). Overall, the average annual ET magnitudes over 2001–11 compare very well with the multimodel ensemble of Yang et al. (2023), except for GRS and CRO, which may be underestimated (Table S10); these differences may partly reflect differences in the underlying

land-cover maps used to estimate aggregated ET values in the various studies.

Global ET trends from this study were also analyzed and compared to the long-term, annual ET records from the C61 baseline and from GLEAM (Fig. 4). ET anomalies were computed by subtracting each product’s 2012–23 mean value, to provide a common period of comparison that includes the shorter VIIRS VNP16 period. All products indicate an increasing trend in global ET consistent with previous studies (Mao et al. 2015; Y. Zhang et al. 2016; Yang et al. 2023) and consistent with well-known, secular changes in climate and in the LAI. At global extent, the increase in annual ET in MOD16 C61 over 2000–11 is 1.54 mm yr^{-2} (p value ≈ 0.001), compared to 0.86 mm yr^{-2} (p value ≈ 0.017) in the updated MOD16

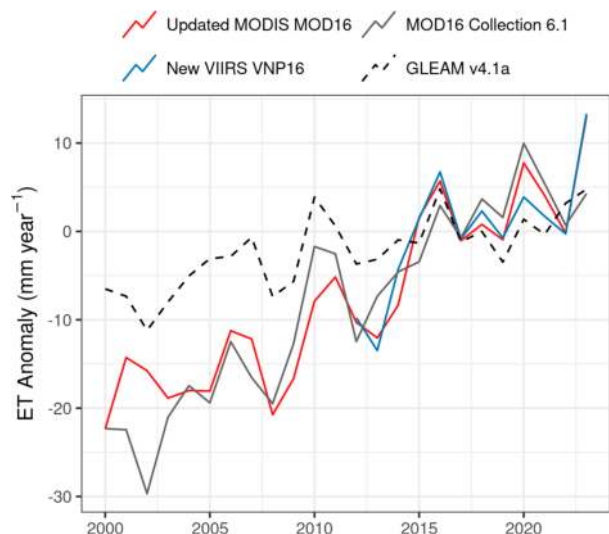


FIG. 4. Annual ET anomalies, relative to the period 2012–23, for MODIS MOD16 and VIIRS VNP16 products, compared to the same from GLEAM, version 4.1a.

product and 0.98 mm yr^{-2} (p value ≈ 0.001) in GLEAM for the same period. This relatively small (and marginally insignificant) rate of increase in this period (2000–11) may reflect a strengthening of water-supply (precipitation-to-PET ratio) constraints on ET (Jung et al. 2010; Zhang et al. 2015), although the short record is also highly uncertain (Anabalón and Sharma 2017).

The ET records also show general consistency in capturing interannual variability (IAV) at global scale, including strong correspondence in trend magnitudes and IAV between the updated MOD16 and VNP16 ET records. While both MOD16 and VNP16 show general consistency in IAV and trends over the long term, a notable difference occurs in 2001–02 where the updated MOD16 results show an increase in annual ET contrasting with the lowest ET anomalies on record from C61 and GLEAM. This difference coincides with regional hydrologic extremes, including widespread drought in the Northern Hemisphere (Lotsch et al. 2005; Zeng et al. 2005) but also localized flooding (Mustafa 2003; Thielen et al. 2005) and may ultimately reflect differences in underlying climate datasets, especially precipitation (Anabalón and Sharma 2017) (GEOS-FP in C61, GEOS-IT in the updated MOD16, and the Global Precipitation Climatology Project in GLEAM). The difference may also reflect different sensitivities to different land domains, based on the underlying EC tower network used; the updated MOD16 uses far more EC towers but most are located in the Northern Hemisphere, where ET IAV has shown less sensitivity to climate oscillations (Miralles et al. 2014).

Over the longer record (2000–23), a faster rate of increase is observed: 1.44 mm yr^{-2} (p value $\ll 0.001$) for MOD16 C61 and 1.24 mm yr^{-2} (p value $\ll 0.001$) for the updated MOD16 compared to 0.43 mm yr^{-2} (p value $\ll 0.001$) for GLEAM. These trends compare well with the range of variability in trends reported by Yang et al. (2023), $0.2\text{--}1.13 \text{ mm yr}^{-2}$ for the period 1982–2011. Croplands exhibit the strongest ET trends but are not solely responsible for the global rise in ET, as previously suggested (Javadian et al. 2020); grasslands, savannas, and DBFs also show rising ET trends over 2001–11 and 2000–23 (Table S11). We find evidence for increasing ET trends among most PFTs in the longer period (2000–23).

The global pattern from the updated MOD16 follows an expected latitudinal and climate variation, but regional trends in ET are revealing (Fig. 5). Consistent with the meta-analysis of Yang et al. (2023), we find strong ET increases in Central Siberia, throughout Europe, and in the humid contiguous United States. Areas of cropland intensification or expansion in China and India stand out as major hotspots of increasing ET, as previously noted (Javadian et al. 2020), although the updated MOD16 presents a more mixed record of trends in South America, North America, and Africa (Fig. 5). Increasing and decreasing ET trends generally coincide with respective trends in pluvial and drought conditions, and vegetation cover (Piao et al. 2020). Notable are widespread ET decreases in Amazonia, southern Africa, and central Australia coinciding with persistent drought in these regions (Du et al. 2021). In the CONUS (Fig. 6), regional ET trends confirm the general southeast-to-northwest contrasts found in the Great Basin associated with differences in elevation (Hall et al. 2023),

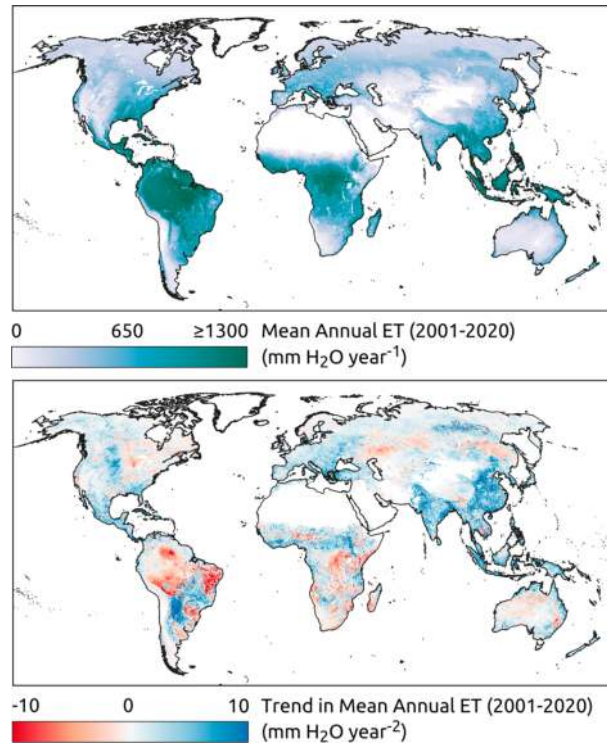


FIG. 5. (top) Mean annual ET and (bottom) trend in mean annual ET, from the updated MOD16, for the period 2001–20.

along with general increases in the southeastern United States (Javadian et al. 2020; Yang et al. 2023).

The advantages of MOD16 include its global extent and moderate (500-m) spatial resolution as well as the ability to combine these observations with other synergistic land products derived from the same sensor and satellite platform. As a regional case study, we combined the updated MOD16 ET estimates with MOD17 global productivity (GPP) estimates (Endsley et al. 2023) to calculate WUE. Here, the WUE metric quantifies the amount of ecosystem carbon (CO_2) uptake from GPP per unit of ET water loss (Beer et al. 2009; De Oliveira et al. 2017) and represents a key linkage between the terrestrial carbon and water cycles. Even at a reduced, 5-km resolution, the combined products reveal complex regional trends in WUE across the CONUS (Fig. 6). Similar to ET, the regional pattern of increasing and decreasing WUE in the CONUS generally follows trends in vegetation cover and water availability (Tercek et al. 2021). WUE trends show a strong spatial autocorrelation, with regional domains including the Great Basin (increasing WUE), the western Great Plains (decreasing WUE), and the croplands of the Midwest (increasing WUE). The global WUE trends from MOD16 and MOD17 are consistent with a reported, general increase in WUE with rising atmospheric CO_2 and vegetation greening (Haverd et al. 2020; Gonsamo et al. 2021; Yang et al. 2023), including widespread enhancement in WUE over southwest CONUS drylands (Fig. 6). The results are also consistent with potential WUE saturation (Li et al. 2023), indicated by strong, significant increases in WUE

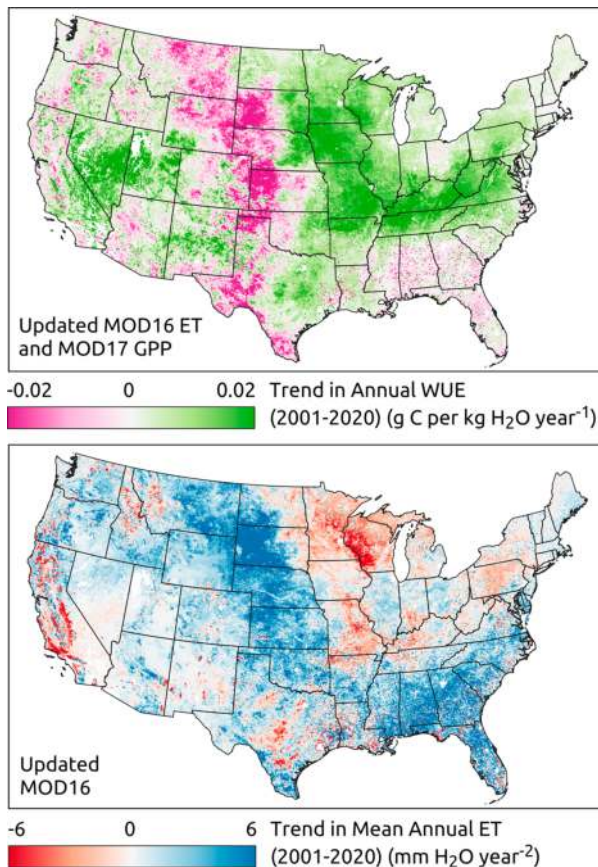


FIG. 6. Trends in (top) annual WUE and (bottom) annual ET, from the updated MOD16 ET product, at 5-km spatial resolution, for the CONUS.

during 2001–11 but weak and insignificant trends over the longer period, 2001–20 (Table S12).

4. Conclusions

In anticipation of the final MODIS MOD16 product release (MODIS Collection 7) and the release of a new, VIIRS VNP16 (with VIIRS Collection 2) ET record, this study presents a comprehensive calibration and validation of the MOD16 terrestrial ET algorithm and the first published improvements to this popular algorithm since Mu et al. (2011). A variety of ground data sources were used to contribute prior information in a Bayesian model-data fusion, where MOD16 parameters were adjusted based on the observed latent heat flux from the largest collection of global EC towers used, to date, in MOD16's calibration. Partitioning of ET, correlation with sapflow data, and an intercomparison with an ensemble of ET models provide further evidence of substantial improvement to the baseline MOD16 algorithm (Mu et al. 2011).

After recalibration, the updated model has lower bias, lower RMSE, and substantially higher correlation and model efficiency than the baseline MOD16 Collection 6.1 (C61). RMSE in latent heat flux improved for all PFTs except

evergreen broadleaf forest (EBF), which has the highest absolute error in MOD16 C61, the updated MOD16, and VNP16 because EBF generally has the highest latent heat fluxes. Correlations with daytime sapflows from SAPFLUXNET range from 0.50 (for DNF) to 0.77 (for MF), excluding WSV, which may not have been properly validated due to limited data for this PFT. A major improvement over the baseline MOD16 C61 was achieved in the partitioning of ET into transpiration (now 71% of ET, on average, based on the median weighted T/ET fraction), soil evaporation (now 16%), and canopy evaporation (now 12%). The increase in transpiration rates and decrease in soil evaporation rates bring the updated MOD16 and new VNP16 in line with multiple prior studies on ET partitioning. Although the published MOD16 and VNP16 data products only report total ET, accurate partitioning is critical for getting this total correct under conditions where soil or canopy evaporation and transpiration might diverge (Stoy et al. 2019; Scott et al. 2021).

Global simulations of ET confirm that ET is highest in the tropics (where EBF is found). Consistent with other reports, mean global ET increased over 2000–23 at a rate of 1.24 mm yr^{-2} , which can largely be attributed to rising ET in croplands, although strong ET trends are observed in GRS, SAV, and DBF as well. By combining MOD16 data with global productivity data from the MODIS MOD17 product, we computed annual, ecosystem WUE magnitudes and trends. We find a general increase in ecosystem WUE during the period 2001–11, compared with negative or much weaker positive trends over the period 2001–20, suggestive of declining gains in WUE. With the new VIIRS VNP16 ET estimates, and the corresponding VIIRS VNP17 GPP and NPP estimates (Endsley et al. 2023), it is now possible to continue this multidecadal, global monitoring of ecosystem water fluxes and WUE through 2030 or later.

Acknowledgments. The authors are grateful for the advice of Forrest Melton (NASA Ames Research Center) and John Volk (Desert Research Institute) on the OpenET model intercomparison. This study was supported by a grant from NASA (80NSSC22K0198). The authors utilized data from AmeriFlux. Funding for the AmeriFlux data portal was provided by the U.S. Department of Energy Office of Science.

Data availability statement. The open-source Python implementation of the MOD16 algorithm is available in Endsley (2024). Global, 5-km simulated ET from the updated MOD16 and new VIIRS VNP16, tower calibration and validation data, and validation data at SAPFLUXNET and OpenET sites can be downloaded from the publicly available archive in Zhao and Endsley (2024).

REFERENCES

- Abbott, P. F., and R. C. Tabony, 1985: The estimation of humidity parameters. *Meteor. Mag.*, **114**, 49–56.
- Abril-Pla, O., and Coauthors, 2023: PyMC: A modern, and comprehensive probabilistic programming framework in Python.

- PeerJ Comput. Sci.*, **9**, e1516, <https://doi.org/10.7717/peerj-cs.1516>.
- Alduchov, O. A., and R. E. Eskridge, 1996: Improved magnus form approximation of saturation vapor pressure. *J. Appl. Meteor.*, **35**, 601–609, [https://doi.org/10.1175/1520-0450\(1996\)035<0601:IMFAOS>2.0.CO;2](https://doi.org/10.1175/1520-0450(1996)035<0601:IMFAOS>2.0.CO;2).
- Anabalón, A., and A. Sharma, 2017: On the divergence of potential and actual evapotranspiration trends: An assessment across alternate global datasets. *Earth's Future*, **5**, 905–917, <https://doi.org/10.1002/2016EF000499>.
- Anderson, M., and Coauthors, 2018: Field-scale assessment of land and water use change over the California delta using remote sensing. *Remote Sens.*, **10**, 889, <https://doi.org/10.3390/rs10060889>.
- Anderson, M. C., J. M. Norman, J. R. Mecikalski, J. A. Otkin, and W. P. Kustas, 2007: A climatological study of evapotranspiration and moisture stress across the continental United States based on thermal remote sensing: 1. Model formulation. *J. Geophys. Res.*, **112**, D10117, <https://doi.org/10.1029/2006JD007506>.
- Beer, C., and Coauthors, 2009: Temporal and among-site variability of inherent water use efficiency at the ecosystem level. *Global Biogeochem. Cycles*, **23**, GB2018, <https://doi.org/10.1029/2008GB003233>.
- Berkelhammer, M., D. C. Noone, T. E. Wong, S. P. Burns, J. F. Knowles, A. Kaushik, P. D. Blanken, and M. W. Williams, 2016: Convergent approaches to determine an ecosystem's transpiration fraction. *Global Biogeochem. Cycles*, **30**, 933–951, <https://doi.org/10.1002/2016GB005392>.
- Bhattarai, N., D. B. Lobell, Balwinder-Singh, R. Fishman, W. P. Kustas, Y. Pokhrel, and M. Jain, 2023: Warming temperatures exacerbate groundwater depletion rates in India. *Sci. Adv.*, **9**, eadi1401, <https://doi.org/10.1126/sciadv.adi1401>.
- Brust, C., J. S. Kimball, M. P. Maneta, K. Jencso, M. He, and R. H. Reichle, 2021: Using SMAP level-4 soil moisture to constrain MOD16 evapotranspiration over the contiguous USA. *Remote Sens. Environ.*, **255**, 112277, <https://doi.org/10.1016/j.rse.2020.112277>.
- Campagnolo, M. L., Q. Sun, Y. Liu, C. Schaaf, Z. Wang, and M. O. Román, 2016: Estimating the effective spatial resolution of the operational BRDF, albedo, and nadir reflectance products from MODIS and VIIRS. *Remote Sens. Environ.*, **175**, 52–64, <https://doi.org/10.1016/j.rse.2015.12.033>.
- Cleugh, H. A., R. Leuning, Q. Mu, and S. W. Running, 2007: Regional evaporation estimates from flux tower and MODIS satellite data. *Remote Sens. Environ.*, **106**, 285–304, <https://doi.org/10.1016/j.rse.2006.07.007>.
- De Oliveira, G., N. A. Brunsell, E. C. Moraes, Y. E. Shimabukuro, G. Bertani, T. V. Dos Santos, and L. E. O. C. Aragao, 2017: Evaluation of MODIS-based estimates of water-use efficiency in Amazonia. *Int. J. Remote Sens.*, **38**, 5291–5309, <https://doi.org/10.1080/01431161.2017.1339924>.
- Du, J., and Coauthors, 2021: Synergistic satellite assessment of global vegetation health in relation to ENSO-induced droughts and pluvials. *J. Geophys. Res. Biogeosci.*, **126**, e2020JG006006, <https://doi.org/10.1029/2020JG006006>.
- Duveiller, G., J. Hooker, and A. Cescatti, 2018: The mark of vegetation change on Earth's surface energy balance. *Nat. Commun.*, **9**, 679, <https://doi.org/10.1038/s41467-017-02810-8>.
- Endsley, K. A., 2024: MOD16 terrestrial evapotranspiration algorithm. Zenodo, accessed 30 October 2024, <https://doi.org/10.5281/ZENODO.12735274>.
- , M. Zhao, J. S. Kimball, and S. Devadiga, 2023: Continuity of global MODIS terrestrial primary productivity estimates in the VIIRS era using model-data fusion. *J. Geophys. Res. Biogeosci.*, **128**, e2023JG007457, <https://doi.org/10.1029/2023JG007457>.
- Fisher, J. B., K. P. Tu, and D. D. Baldocchi, 2008: Global estimates of the land-atmosphere water flux based on monthly AVHRR and ISLSCP-II data, validated at 16 FLUXNET sites. *Remote Sens. Environ.*, **112**, 901–919, <https://doi.org/10.1016/j.rse.2007.06.025>.
- Friedl, M., and D. Sulla-Menashe, 2019: MCD12Q1MODIS/Terra+Aqua Land Cover Type Yearly L3 Global 500m SIN Grid V006 [Data set]. NASA EOSDIS Land Processes Distributed Active Archive Center, accessed 18 October 2021, <https://doi.org/10.5067/MODIS/MCD12Q1.006>.
- Gelaro, R., and Coauthors, 2017: The Modern-Era Retrospective Analysis for Research and Applications, version 2 (MERRA-2). *J. Climate*, **30**, 5419–5454, <https://doi.org/10.1175/JCLI-D-16-0758.1>.
- Gonsamo, A., and Coauthors, 2021: Greening drylands despite warming consistent with carbon dioxide fertilization effect. *Global Change Biol.*, **27**, 3336–3349, <https://doi.org/10.1111/gcb.15658>.
- Good, S. P., D. Noone, and G. Bowen, 2015: Hydrologic connectivity constrains partitioning of global terrestrial water fluxes. *Science*, **349**, 175–177, <https://doi.org/10.1126/science.aaa5931>.
- Greve, P., B. Orłowsky, B. Mueller, J. Sheffield, M. Reichstein, and S. I. Seneviratne, 2014: Global assessment of trends in wetting and drying over land. *Nat. Geosci.*, **7**, 716–721, <https://doi.org/10.1038/ngeo2247>.
- Gupta, H. V., and H. Kling, 2011: On typical range, sensitivity, and normalization of mean squared error and Nash-Sutcliffe efficiency type metrics. *Water Resour. Res.*, **47**, W10601, <https://doi.org/10.1029/2011WR010962>.
- Hall, D. K., J. S. Kimball, R. Larson, N. E. DiGirolamo, K. A. Casey, and G. Hulley, 2023: Intensified warming and aridity accelerate terminal lake desiccation in the Great Basin of the western United States. *Earth Space Sci.*, **10**, e2022EA002630, <https://doi.org/10.1029/2022EA002630>.
- Haverd, V., and Coauthors, 2020: Higher than expected CO₂ fertilization inferred from leaf to global observations. *Global Change Biol.*, **26**, 2390–2402, <https://doi.org/10.1111/gcb.14950>.
- He, M., J. S. Kimball, Y. Yi, S. W. Running, K. Guan, A. Moreno, X. Wu, and M. Maneta, 2019: Satellite data-driven modeling of field scale evapotranspiration in croplands using the MOD16 algorithm framework. *Remote Sens. Environ.*, **230**, 111201, <https://doi.org/10.1016/j.rse.2019.05.020>.
- Huang, J., H. Yu, X. Guan, G. Wang, and R. Guo, 2016: Accelerated dryland expansion under climate change. *Nat. Climate Change*, **6**, 166–171, <https://doi.org/10.1038/nclimate2837>.
- Huntington, T. G., 2006: Evidence for intensification of the global water cycle: Review and synthesis. *J. Hydrol.*, **319**, 83–95, <https://doi.org/10.1016/j.jhydrol.2005.07.003>.
- Iribane, J. V., and W. L. Godson, 1981: *Atmospheric Thermodynamics*. 2nd ed. D. Reidel Publishing Company, 260 pp.
- Javadian, M., A. Behrang, W. K. Smith, and J. B. Fisher, 2020: Global trends in evapotranspiration dominated by increases across large cropland regions. *Remote Sens.*, **12**, 1221, <https://doi.org/10.3390/rs12071221>.
- Jung, M., and Coauthors, 2010: Recent decline in the global land evapotranspiration trend due to limited moisture supply. *Nature*, **467**, 951–954, <https://doi.org/10.1038/nature09396>.
- Justice, C. O., J. R. G. Townshend, E. F. Vermote, E. Masuoka, R. E. Wolfe, N. Saleous, D. P. Roy, and J. T. Morisette,

- 2002: An overview of MODIS Land data processing and product status. *Remote Sens. Environ.*, **83**, 3–15, [https://doi.org/10.1016/S0034-4257\(02\)00084-6](https://doi.org/10.1016/S0034-4257(02)00084-6).
- Kattge, J., and Coauthors, 2020: TRY plant trait database—Enhanced coverage and open access. *Global Change Biol.*, **26**, 119–188, <https://doi.org/10.1111/gcb.14904>.
- Kilic, A., R. G. Allen, P. Blankenau, P. Revelle, D. Ozturk, and J. Huntington, 2021: Global production and free access to landsat-scale evapotranspiration with EEFlux and eeMETRIC. *Sixth Decennial National Irrigation Symp.*, 6–8, December 2021, San Diego, CA, American Society of Agricultural and Biological Engineers, <https://doi.org/10.13031/irrig.2020-038>.
- Laipelt, L., R. Henrique Bloedow Kayser, A. Santos Fleischmann, A. Ruhoff, W. Bastiaanssen, T. A. Erickson, and F. Melton, 2021: Long-term monitoring of evapotranspiration using the SEBAL algorithm and Google Earth Engine cloud computing. *ISPRS J. Photogramm. Remote Sens.*, **178**, 81–96, <https://doi.org/10.1016/j.isprsjrs.2021.05.018>.
- Li, F., J. Xiao, J. Chen, A. Ballantyne, K. Jin, B. Li, M. Abraha, and R. John, 2023: Global water use efficiency saturation due to increased vapor pressure deficit. *Science*, **381**, 672–677, <https://doi.org/10.1126/science.adf5041>.
- Li, Y., M. Zhao, S. Motesharrei, Q. Mu, E. Kalnay, and S. Li, 2015: Local cooling and warming effects of forests based on satellite observations. *Nat. Commun.*, **6**, 6603, <https://doi.org/10.1038/ncomms7603>.
- Liang, S., and Coauthors, 2021: The Global Land Surface Satellite (GLASS) product suite. *Bull. Amer. Meteor. Soc.*, **102**, E323–E337, <https://doi.org/10.1175/BAMS-D-18-0341.1>.
- Liu, Y., and Coauthors, 2017: Evaluation of the VIIRS BRDF, Albedo and NBAR products suite and an assessment of continuity with the long term MODIS record. *Remote Sens. Environ.*, **201**, 256–274, <https://doi.org/10.1016/j.rse.2017.09.020>.
- Lotsch, A., M. A. Friedl, B. T. Anderson, and C. J. Tucker, 2005: Response of terrestrial ecosystems to recent Northern Hemispheric drought. *Geophys. Res. Lett.*, **32**, L06705, <https://doi.org/10.1029/2004GL022043>.
- Mao, J., and Coauthors, 2015: Disentangling climatic and anthropogenic controls on global terrestrial evapotranspiration trends. *Environ. Res. Lett.*, **10**, 094008, <https://doi.org/10.1088/1748-9326/10/9/094008>.
- McDowell, N. G., and Coauthors, 2022: Mechanisms of woody-plant mortality under rising drought, CO₂ and vapour pressure deficit. *Nat. Rev. Earth Environ.*, **3**, 294–308, <https://doi.org/10.1038/s43017-022-00272-1>.
- Melton, F. S., L. F. Johnson, C. P. Lund, L. L. Pierce, A. R. Michaelis, and S. H. Hiatt, 2012: Satellite irrigation management support with the terrestrial observation and prediction system: A framework for integration of satellite and surface observations to support improvements in agricultural water resource management. *IEEE J. Sel. Top. Appl. Earth Obs. Remote Sens.*, **5**, 1709–1721, <https://doi.org/10.1109/JSTARS.2012.2214474>.
- , and Coauthors, 2022: OpenET: Filling a critical data gap in water management for the western United States. *J. Amer. Water Resour. Assoc.*, **58**, 971–994, <https://doi.org/10.1111/1752-1688.12956>.
- Miralles, D. G., and Coauthors, 2014: El Niño–La Niña cycle and recent trends in continental evaporation. *Nat. Climate Change*, **4**, 122–126, <https://doi.org/10.1038/nclimate2068>.
- , and Coauthors, 2025: GLEAM4: Global land evaporation and soil moisture dataset at 0.1° resolution from 1980 to near present. *Sci. Data*, **12**, 416, <https://doi.org/10.1038/s41597-025-04610-y>.
- Monteith, J. L., 1965: Evaporation and environment. *Symp. Soc. Exp. Biol.*, **19**, 205–234.
- Mu, Q., F. A. Heinsch, M. Zhao, and S. W. Running, 2007: Development of a global evapotranspiration algorithm based on MODIS and global meteorology data. *Remote Sens. Environ.*, **111**, 519–536, <https://doi.org/10.1016/j.rse.2007.04.015>.
- , M. Zhao, and S. W. Running, 2011: Improvements to a MODIS global terrestrial evapotranspiration algorithm. *Remote Sens. Environ.*, **115**, 1781–1800, <https://doi.org/10.1016/j.rse.2011.02.019>.
- Mustafa, D., 2003: Reinforcing vulnerability? Disaster relief, recovery, and response to the 2001 flood in Rawalpindi, Pakistan. *Global Environ. Change*, **5B**, 71–82, <https://doi.org/10.1016/j.hazards.2004.05.001>.
- Myneni, R., and Y. Knyazikhin, 2018: VIIRS/NPP Leaf Area Index/FPAR 8-Day L4 Global 500m SIN Grid V001. NASA EOSDIS Land Processes Distributed Active Archive Center, accessed 15 August 2023, <https://doi.org/10.5067/VIIRS/VNP15A2H.001>.
- Myneni, R. B., and Coauthors, 2002: Global products of vegetation leaf area and fraction absorbed PAR from year one of MODIS data. *Remote Sens. Environ.*, **83**, 214–231, [https://doi.org/10.1016/S0034-4257\(02\)00074-3](https://doi.org/10.1016/S0034-4257(02)00074-3).
- NASA, 2019: GPM IMERG Final Precipitation L3 1 day 0.1 degree x 0.1 degree V06. NASA Goddard Earth Sciences Data and Information Services Center, accessed 13 February 2024, <https://doi.org/10.5067/GPM/IMERGDF/DAY06>.
- NASA-JPL, 2013: NASA Shuttle Radar Topography Mission Global 30 arc second. NASA EOSDIS Land Processes Distributed Active Archive Center, accessed 15 August 2023, <https://doi.org/10.5067/MEaSUREs/SRTM/SRTMGL30.002>.
- National Physical Laboratory, 2002: Buoyancy correction and air density measurement. NPL Tech. Rep., 4 pp., https://resource.npl.co.uk/docs/science_technology/mass_force_pressure/clubs_groups/instmc_weighting_panel/buoycornote.pdf.
- Newbold, T., and Coauthors, 2016: Has land use pushed terrestrial biodiversity beyond the planetary boundary? A global assessment. *Science*, **353**, 288–291, <https://doi.org/10.1126/science.aaf2201>.
- Oki, T., and S. Kanae, 2006: Global hydrological cycles and world water resources. *Science*, **313**, 1068–1072, <https://doi.org/10.1126/science.1128845>.
- Pastorello, G., and Coauthors, 2020: The FLUXNET2015 dataset and the ONEFlux processing pipeline for eddy covariance data. *Sci. Data*, **7**, 225, <https://doi.org/10.1038/s41597-020-0534-3>.
- Paulus, S. J., and Coauthors, 2024: Interpretability of negative latent heat fluxes from eddy covariance measurements in dry conditions. *Biogeosciences*, **21**, 2051–2085, <https://doi.org/10.5194/bg-21-2051-2024>.
- Piao, S., and Coauthors, 2020: Characteristics, drivers and feedbacks of global greening. *Nat. Rev. Earth Environ.*, **1**, 14–27, <https://doi.org/10.1038/s43017-019-0001-x>.
- Poyatos, R., and Coauthors, 2021: Global transpiration data from sap flow measurements: The SAPFLUXNET database. *Earth Syst. Sci. Data*, **13**, 2607–2649, <https://doi.org/10.5194/essd-2020-227>.
- Rigden, A. J., G. D. Salvucci, D. Entekhabi, and D. J. Short Gianotti, 2018: Partitioning evapotranspiration over the continental United States using weather station data. *Geophys. Res. Lett.*, **45**, 9605–9613, <https://doi.org/10.1029/2018GL079121>.

- Román, M. O., and Coauthors, 2024: Continuity between NASA MODIS Collection 6.1 and VIIRS Collection 2 land products. *Remote Sens. Environ.*, **302**, 113963, <https://doi.org/10.1016/j.rse.2023.113963>.
- Running, S. W., Q. Mu, M. Zhao, and A. Moreno, 2021: User's Guide: MODIS Global Terrestrial Evapotranspiration (ET) Product (NASA MOD16A2/A3) NASA Earth Observing System MODIS Land Algorithm (For Collection 6.1). MODIS Land Team Tech. Rep. 34 pp.
- Schaaf, C., and Z. Wang, 2021: MODIS/Terra+Aqua BRDF/Albedo Daily L3 Global—500m V061. NASA EOSDIS Land Processes Distributed Active Archive Center, accessed 17 July 2024, <https://doi.org/10.5067/MODIS/MCD43A3.061>.
- , —, X. Zhang, and A. Strahler, 2018: VIIRS/NPP BRDF/Albedo Model Parameters Daily L3 Global 1 km SIN Grid V001. NASA EOSDIS Land Processes Distributed Active Archive Center, accessed 17 July 2024, <https://doi.org/10.5067/VIIRS/VNP43MA1.001>.
- Schlesinger, W. H., and S. Jasechko, 2014: Transpiration in the global water cycle. *Agric. For. Meteorol.*, **189–190**, 115–117, <https://doi.org/10.1016/j.agrformet.2014.01.011>.
- Scott, R. L., J. F. Knowles, J. A. Nelson, P. Gentine, X. Li, G. Barron-Gafford, R. Bryant, and J. A. Biederman, 2021: Water availability impacts on evapotranspiration partitioning. *Agric. For. Meteorol.*, **297**, 108251, <https://doi.org/10.1016/j.agrformet.2020.108251>.
- Seddon, A. W. R., M. Macias-Fauria, P. R. Long, D. Benz, and K. J. Willis, 2016: Sensitivity of global terrestrial ecosystems to climate variability. *Nature*, **531**, 229–232, <https://doi.org/10.1038/nature16986>.
- Senay, G. B., and Coauthors, 2023: Improving the operational simplified surface energy balance evapotranspiration model using the forcing and normalizing operation. *Remote Sens.*, **15**, 260, <https://doi.org/10.3390/rs15010260>.
- Smith, A. A., C. Welch, and T. A. Stadnyk, 2018: Assessing the seasonality and uncertainty in evapotranspiration partitioning using a tracer-aided model. *J. Hydrol.*, **560**, 595–613, <https://doi.org/10.1016/j.jhydrol.2018.03.036>.
- Stoy, P. C., and Coauthors, 2019: Reviews and syntheses: Turning the challenges of partitioning ecosystem evaporation and transpiration into opportunities. *Biogeosciences*, **16**, 3747–3775, <https://doi.org/10.5194/bg-16-3747-2019>.
- Sulla-Menashe, D., J. M. Gray, S. P. Abercrombie, and M. A. Friedl, 2019: Hierarchical mapping of annual global land cover 2001 to present: The MODIS collection 6 land cover product. *Remote Sens. Environ.*, **222**, 183–194, <https://doi.org/10.1016/j.rse.2018.12.013>.
- Talsma, C. J., S. P. Good, C. Jimenez, B. Martens, J. B. Fisher, D. G. Miralles, M. F. McCabe, and A. J. Purdy, 2018: Partitioning of evapotranspiration in remote sensing-based models. *Agric. For. Meteorol.*, **260–261**, 131–143, <https://doi.org/10.1016/j.agrformet.2018.05.010>.
- Ter Braak, C. J. F., and J. A. Vrugt, 2008: Differential evolution Markov Chain with snooker updater and fewer chains. *Stat. Comput.*, **18**, 435–446, <https://doi.org/10.1007/s11222-008-9104-9>.
- Tercek, M. T., D. Thoma, J. E. Gross, K. Sherrill, S. Kagone, and G. Senay, 2021: Historical changes in plant water use and need in the continental United States. *PLOS ONE.*, **16**, e0256586, <https://doi.org/10.1371/journal.pone.0256586>.
- Thielen, A. H., M. Müller, H. Kreibich, and B. Merz, 2005: Flood damage and influencing factors: New insights from the August 2002 flood in Germany. *Water Resour. Res.*, **41**, W12430, <https://doi.org/10.1029/2005WR004177>.
- Trenberth, K. E., L. Smith, T. Qian, A. Dai, and J. Fasullo, 2007: Estimates of the global water budget and its annual cycle using observational and model data. *J. Hydrometeorol.*, **8**, 758–769, <https://doi.org/10.1175/JHM600.1>.
- van de Griend, A. A., and M. Owe, 1994: Bare soil surface resistance to evaporation by vapor diffusion under semiarid conditions. *Water Resour. Res.*, **30**, 181–188, <https://doi.org/10.1029/93WR02747>.
- Volk, J. M., and Coauthors, 2023a: OpenET model data for assessing the accuracy of OpenET satellite-based evapotranspiration data to support water resource and land management applications. Zenodo, accessed 23 September 2024, <https://doi.org/10.5281/ZENODO.10119477>.
- , and Coauthors, 2023b: Post-processed data and graphical tools for a CONUS-wide eddy flux evapotranspiration dataset. Zenodo, accessed 23 September 2024, <https://doi.org/10.5281/ZENODO.7636781>.
- , and Coauthors, 2024: Assessing the accuracy of OpenET satellite-based evapotranspiration data to support water resource and land management applications. *Nat. Water*, **2**, 193–205, <https://doi.org/10.1038/s44221-023-00181-7>.
- Wei, Z., K. Yoshimura, L. Wang, D. G. Miralles, S. Jasechko, and X. Lee, 2017: Revisiting the contribution of transpiration to global terrestrial evapotranspiration. *Geophys. Res. Lett.*, **44**, 2792–2801, <https://doi.org/10.1002/2016GL072235>.
- Wiecki, T., and Coauthors, 2024: PyMC-devs/pymc: V5.16.1. Zenodo, accessed 1 June 2022, <https://doi.org/10.5281/ZENODO.4603970>.
- Wild, M., D. Folini, C. Schär, N. Loeb, E. G. Dutton, and G. König-Langlo, 2013: The global energy balance from a surface perspective. *Climate Dyn.*, **40**, 3107–3134, <https://doi.org/10.1007/s00382-012-1569-8>.
- Wullschlegel, S. D., P. J. Hanson, and D. E. Todd, 2001: Transpiration from a multi-species deciduous forest as estimated by xylem sap flow techniques. *For. Ecol. Manage.*, **143**, 205–213, [https://doi.org/10.1016/S0378-1127\(00\)00518-1](https://doi.org/10.1016/S0378-1127(00)00518-1).
- Xu, B., and Coauthors, 2018: Analysis of global LAI/FPAR products from VIIRS and MODIS sensors for spatio-temporal consistency and uncertainty from 2012–2016. *Forests*, **9**, 73, <https://doi.org/10.3390/f9020073>.
- Xu, C., N. G. McDowell, R. A. Fisher, L. Wei, S. Sevanto, B. O. Christoffersen, E. Weng, and R. S. Middleton, 2019: Increasing impacts of extreme droughts on vegetation productivity under climate change. *Nat. Climate Change*, **9**, 948–953, <https://doi.org/10.1038/s41558-019-0630-6>.
- Yan, K., and Coauthors, 2021: Performance stability of the MODIS and VIIRS LAI algorithms inferred from analysis of long time series of products. *Remote Sens. Environ.*, **260**, 112438, <https://doi.org/10.1016/j.rse.2021.112438>.
- Yang, Y., and Coauthors, 2023: Evapotranspiration on a greening Earth. *Nat. Rev. Earth Environ.*, **4**, 626–641, <https://doi.org/10.1038/s43017-023-00464-3>.
- Zeng, N., H. Qian, C. Roedenbeck, and M. Heimann, 2005: Impact of 1998–2002 midlatitude drought and warming on terrestrial ecosystem and the global carbon cycle. *Geophys. Res. Lett.*, **32**, L22709, <https://doi.org/10.1029/2005GL024607>.
- Zhang, K., J. S. Kimball, R. R. Nemani, S. W. Running, Y. Hong, J. J. Gourley, and Z. Yu, 2015: Vegetation greening and climate change promote multidecadal rises of global land evapotranspiration. *Sci. Rep.*, **5**, 15956, <https://doi.org/10.1038/srep15956>.
- , —, and S. W. Running, 2016: A review of remote sensing based actual evapotranspiration estimation. *Wiley Interdiscip. Rev.: Water*, **3**, 834–853, <https://doi.org/10.1002/wat2.1168>.

- , G. Zhu, J. Ma, Y. Yang, S. Shang, and C. Gu, 2019: Parameter analysis and estimates for the MODIS evapotranspiration algorithm and multiscale verification. *Water Resour. Res.*, **55**, 2211–2231, <https://doi.org/10.1029/2018WR023485>.
- Zhang, Y., and Coauthors, 2016: Multi-decadal trends in global terrestrial evapotranspiration and its components. *Sci. Rep.*, **6**, 19124, <https://doi.org/10.1038/srep19124>.
- , and Coauthors, 2023: Southern Hemisphere dominates recent decline in global water availability. *Science*, **382**, 579–584, <https://doi.org/10.1126/science.adh0716>.
- Zhao, M., and K. A. Endsley, 2024: Global evapotranspiration estimates and calibration, validation data for “Improved global estimates of terrestrial evapotranspiration using the MODIS and VIIRS sensors”. Zenodo, accessed 24 October 2024, <https://doi.org/10.5281/ZENODO.13988805>.
- , F. A. Heinsch, R. R. Nemani, and S. W. Running, 2005: Improvements of the MODIS terrestrial gross and net primary production global data set. *Remote Sens. Environ.*, **95**, 164–176, <https://doi.org/10.1016/j.rse.2004.12.011>.
- Zhou, S., B. Yu, Y. Zhang, Y. Huang, and G. Wang, 2016: Partitioning evapotranspiration based on the concept of underlying water use efficiency. *Water Resour. Res.*, **52**, 1160–1175, <https://doi.org/10.1002/2015WR017766>.